methane

MDPI

Article

Harnessing Nitrous Oxide for Sustainable Methane Activation: A Computational Exploration of CNC-Ligated Iron Catalysts

Bruce M. Prince

Center for Catalysis Computational Research (3CR), Department of Chemistry, Texas Southern University, 3100 Cleburne Street, Houston, TX 77004, USA; bruce.prince@tsu.edu

Abstract: This study employs DFT at the APFD/def2-TZVP level, with SMD solvation in THF, to investigate the catalytic activation of methane by $[(\kappa^3\text{-CNC})Fe(N_2O)]^{2+}$ cation complexes. The catalytic mechanism encompasses three key steps: oxygen atom transfer (OAT), hydrogen atom abstraction (HAA), and oxygen radical rebound (ORR). The computational results identify OAT as the rate-determining step, with activation barriers of −10.2 kcal/mol and 5.0 kcal/mol for κ^1-O- and κ^1-N-bound intermediates in the gas and solvent phases, respectively. Methane activation proceeds via HAA, with energy barriers of 16.0–25.2 kcal/mol depending on the spin state and solvation, followed by ORR, which occurs efficiently with barriers as low as 6.4 kcal/mol. The triplet (S = 1) and quintet (S = 2) spin states exhibit critical roles in the catalytic pathway, with intersystem crossing facilitating optimal reactivity. Spin density analysis highlights the oxyl radical character of the Fe^{IV}=O intermediate as being essential for activating methane's strong C–H bond. These findings underscore the catalytic potential of CNC-ligated iron complexes for methane functionalization and demonstrate their dual environmental benefits by utilizing methane and reducing nitrous oxide, a potent greenhouse gas.

Keywords: iron–oxo; iron–oxyl; oxo–cation; methane carbon–hydrogen activation; radical; oxygen radical rebound; methanol; oxo; oxyl; hydrogen atom abstraction; HAA; hydrogen atom transfer; HAT; intersystem crossing

Academic Editor: Patrick Da Costa

Received: 17 January 2025
Revised: 13 February 2025
Accepted: 24 February 2025
Published: 5 March 2025

Citation: Prince, B.M. Harnessing Nitrous Oxide for Sustainable Methane Activation: A Computational Exploration of CNC-Ligated Iron Catalysts. *Methane* **2025**, *4*, 6. https://doi.org/10.3390/methane4010006

1. Introduction

The catalytic transformation of methane [1–5], a critical yet challenging step in chemical synthesis, holds promise for producing value-added chemicals like methanol [5–13]. Despite its abundance and potential as a versatile feedstock, methane's high carbon–hydrogen (C–H) bond dissociation enthalpy (BDE) (~105 kcal/mol) makes its functionalization energetically demanding [1–5,14–17]. This challenge has driven significant research into developing efficient catalysts capable of overcoming this barrier under mild conditions [18,19].

Simultaneously, nitrous oxide (N_2O), which is a potent greenhouse gas with a global warming potential approximately 300 times greater than carbon dioxide, possesses a significant environmental challenge [20–24]. Emissions of N_2O originate from both natural sources, such as microbial soil and ocean activity, and anthropogenic activities like agricultural fertilization and industrial processes. Beyond its contribution to climate change, N_2O is a known ozone-depleting substance, emphasizing the urgent need for mitigation strategies [25–29].

Catalysts capable of utilizing N_2O as an oxidant for methane activation offer the following dual benefits: ref. [30] reducing N_2O concentrations while achieving selective methane functionalization [30]. The thermodynamic properties of N_2O make it an attractive oxygen donor, with its Gibbs free energy of dissociation ($\Delta G = -19$ kcal/mol) indicating a

favorable oxygen atom transfer (OAT) [31–34]. The strong N≡N bond (bond dissociation enthalpy = 113 kcal/mol) and weaker N–O bond (~39 kcal/mol) suggest that N_2O can effectively participate in catalytic cycles involving oxygen transfer [35–37].

Among the potential catalysts, transition metal complexes supported by pyridine(dicarbene)pincer (κ^3-CNC) ligands have emerged as promising candidates [38]. These ligands, derived from N-heterocyclic carbenes (NHCs), exhibit strong σ-donating and π-accepting properties, stabilizing high-valent metal species essential for challenging transformations [39–49]. A specific focus of this study is the simplified CNC ligand framework, which omits BR_2 appendages [44]. This design enables direct comparisons with previously studied systems, such as the BR_2-functionalized CNC ligands explored by Kiernicki et al. and Zimmer et al. [44,45,50]. Kiernicki's work investigated CNC ligands with bulky allyl and BR_2 [44] groups to examine their steric and electronic effects on iron-mediated transformations, while Zimmer and Danopoulos analyzed similar systems in the context of small-molecule activation [44,45,51]. These prior studies provided valuable insights into ligand modifications but introduced steric hindrance and competing interactions that may have obscured the primary coordination effects, for example, C-H activation [13].

The simplified CNC ligand design in this study offers several advantages:

1. Electronic Flexibility: The CNC framework offers strong σ-donation and π-acceptance, stabilizing high-valent iron–oxo intermediates crucial for OAT and methane C–H activation. The absence of BR_2 groups eliminates potential electronic interferences, allowing the study to focus on primary metal–ligand interactions [52].
2. Steric Profile: Excluding bulky BR_2 substituents ensures a compact coordination environment around the iron center. This steric simplicity reduces hindrance at the active site, facilitating efficient catalytic turnover [44].
3. Catalyst Modularity: The simplified ligand design enables direct comparisons with previously studied systems that include BR_2 groups, isolating the effects of the primary coordination sphere. This approach provides clearer mechanistic insights into the role of the Fe center [53].
4. Suitability for High-Valent Oxo Complexes: The CNC ligand's electronic properties support the stabilization of Fe^{IV}=O intermediates, which are critical for methane C–H activation. Excluding BR_2 substituents avoids secondary interactions that might introduce competing pathways, simplifying mechanistic investigations [31,54–58].

These attributes make the CNC-ligated iron complexes ideal candidates for exploring methane activation and nitrous oxide utilization under mild conditions [53], as shown in Scheme 1. This study employs density functional theory (DFT) to investigate the catalytic potential of $[(\kappa^3\text{-CNC})Fe(N_2O)]^{2+}$ complexes, as summarized in Scheme 1 [38]. The mechanism involves three key steps: OAT [9,31–34], hydrogen atom abstraction (HAA) [59–67], and oxygen radical rebound (ORR) [68–70], which is facilitated by high-valent Fe^{IV}=O intermediates. Spin-state dynamics, including intersystem crossing (ISC) between quintet (S = 2) and triplet (S = 1) states, play a central role in determining reaction energetics.

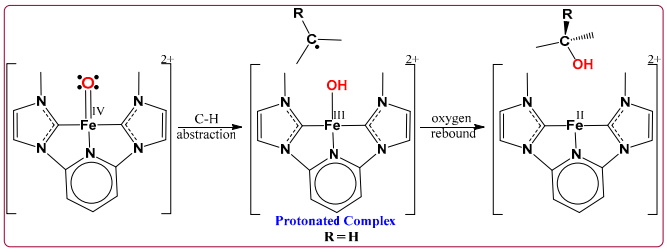

Scheme 1. General reaction cycle for methane C–H activation via $[(\kappa^3\text{-CNC})Fe(N2O)]^{2+}$ complexes, involving OAT, HAA, and ORR. The oxygen atom of N_2O is coordinated trans to the pyridine nitrogen atom of the κ^3-CNC ligand, facilitating C–H activation.

Through Computational Modeling, This Research Aims to Achieve the Following

1. Examine the impact of spin states on methane activation pathways.
2. Assess the activation barriers for the OAT, HAA, and ORR steps.
3. Explore the role of CNC ligands in stabilizing reactive intermediates and facilitating efficient catalysis.

By addressing the dual challenges of methane activation and N_2O mitigation, this work offers insights into sustainable catalytic processes that align with environmental and industrial goals. Scheme 2 outlines the proposed catalytic pathway for methane C–H activation, highlighting the energetic barriers for each step. The complete reaction mechanism and its spin-state-dependent energetics are depicted in Scheme 2.

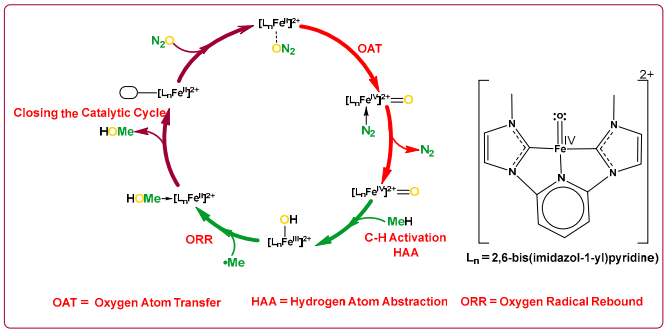

Scheme 2. Proposed catalytic pathway for methane functionalization by $[(\kappa^3\text{-CNC})Fe(N_2O)]^{2+}$ complexes, including key transition states for OAT, HAA, and ORR. Energetics are calculated for singlet, triplet, and quintet spin states.

2. Computational Methods

This study employed density functional theory (DFT) calculations to investigate the methane C–H activation [71] mechanism mediated by $[(\kappa^3\text{-CNC})Fe^{II}(N_2O)]^{2+}$ cation complexes. The methodology was designed to provide a comprehensive understanding of reaction energetics, spin-state dynamics, and mechanistic pathways.

2.1. Level of Theory

The Austin–Frisch–Petersson functional with dispersion corrections (APFD) was used in combination with the def2-TZVP basis set for all geometry optimizations and single-point energy calculations. The APFD functional was selected due to its proven reliability in modeling transition metal complexes, particularly those involving high-valent iron species and non-covalent interactions [72,73].

Unlike traditional functionals such as B3LYP [74–76] or M06 [77], which often require additional empirical dispersion corrections (e.g., Grimme's D3 correction), APFD [73] natively incorporates dispersion effects, ensuring a consistent and accurate treatment of long-range interactions. Dispersion interactions play a critical role in stabilizing intermediates and transition states in the catalytic cycle, particularly during steps such as OAT, HAA, and ORR. The TSs were authenticated using the intrinsic reaction coordinate (IRC) method [78].

APFD [73] also excels in capturing subtle electronic energy differences between spin states, which is essential for this study given the importance of ISC between quintet (S = 2) and triplet (S = 1) states. These spin-state transitions heavily influence the reaction energetics and mechanistic pathways of methane activation and nitrous oxide utilization. By contrast, B3LYP [74] and M06 [77] have demonstrated limitations in accurately describing high-spin systems or the energetics of multi-reference states without significant adjustments [73,79].

Moreover, APFD [73] combines computational efficiency with accuracy, making it suitable for the extensive modeling of large and complex systems like CNC-ligated iron complexes. The functional's compatibility with the SMD [80] implicit solvation model further enhances its applicability to reactions in polar solvents such as THF (ε = 7.4257), which plays a crucial role in stabilizing charged species and transition states.

2.2. Geometric Optimization and Frequency Analysis

All geometries, including intermediates and transition states, were optimized at the APFD/def2-TZVPAnonymous [73] level using fine numerical integration grids and tight convergence criteria. Frequency analysis was performed to confirm the nature of each stationary point, with the minima exhibiting no imaginary frequencies and the transition states showing a single imaginary frequency corresponding to the reaction coordinate. IRC calculations were conducted to validate the connectivity between reactants, transition states, and products [78,81].

2.3. Spin-State Considerations

To explore the role of spin multiplicity in the reaction pathways, calculations were performed for the singlet (S = 0), triplet (S = 1), and quintet (S = 2) spin states at each step of the reaction. Mulliken population analysis was employed to analyze spin density distributions and electronic configurations, providing insights into the localization of unpaired electrons. ISC pathways were evaluated to assess their influence on reaction energetics and spin-state transitions.

2.4. Energetic Calculations

Gibbs free energies (ΔG) were computed at 298.15 K and 1 atm, incorporating thermal corrections and solvation effects. The energies were reported relative to the separated reactants (NHC-Fe + N_2O and NHC-Fe=O + CH_4). The relative Gibbs free energy profiles were used to identify the rate-determining steps and evaluate the overall feasibility of the catalytic pathways.

2.5. Computational Model

The pyridine(dicarbene)pincer (κ^3-CNC) ligand was modeled with methyl substituents on the nitrogen atoms to reduce the computational cost while preserving the ligand's electronic properties. This simplified model allowed for the accurate investigation of the catalytic system, focusing on the primary coordination environment of the Fe center [44,46,82,83].

2.6. Reaction Pathways Investigated

The study examined three critical steps in methane activation:

1. Oxygen Atom Transfer (OAT): Coordination of N_2O to the Fe center and oxygen atom transfer to form the high-valent Fe^{IV}=O intermediate.
2. Hydrogen Atom Abstraction (HAA): Interaction of the Fe^{IV}=O species with methane to cleave the C–H bond.
3. Oxygen Radical Rebound (ORR): Rebound of the hydroxyl group with the methyl radical to yield methanol.

2.7. Software and Computational Resources

All calculations were performed using the Gaussian 16 software suite with access to high-performance computing resources [72]. The Cartesian coordinates of all optimized geometries and the corresponding calculated energy values are provided in the Supporting Information (SI).

3. Results and Discussion

3.1. [(CNC)Fe^{II}]$^{2+}$ Cation Complexes

The [(κ^3-CNC)Fe^{II}]$^{2+}$ cation complex serves as the foundational structure for the catalytic cycle, with its geometric and electronic properties providing critical insights into reactivity. The optimized geometries for the singlet (S = 0), triplet (S = 1), and quintet (S = 2) spin states reveal significant differences in bond lengths, bond angles, and spin density distributions, as summarized in Figure 1 and Table 1.

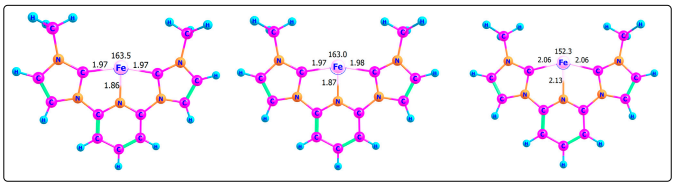

Figure 1. Optimized geometries of [(κ^3-CNC)Fe^{II}]$^{2+}$ cation complexes in singlet (S = 0), triplet (S = 1), and quintet (S = 2) spin states, respectively. Bond lengths are given in Å, and bond angles in degrees. The quintet state shows longer bond lengths and wider angles, reflecting the influence of spin multiplicity on molecular geometry.

Table 1. Key geometric parameters (bond lengths in Å, bond angles in degrees) and spin density distributions (e$^-$) for [(κ^3-CNC)Fe^{II}]$^{2+}$ cation complexes across singlet (S = 0), triplet (S = 1), and quintet (S = 2) spin states.

Spin State	Fe–C (Å)	Fe–N (Å)	C–Fe–C (°)	Spin Density (Fe, e$^-$)
Singlet (S = 0)	1.97	1.86	163.5	0.00
Triplet (S = 1)	1.97	1.87	163.0	2.17
Quintet (S = 2)	2.06	2.13	152.3	4.00

3.2. Geometric and Spin-State Analysis

The geometric parameters of the [(κ^3-CNC)Fe]$^{2+}$ complex reveal significant variations across the quintet (S = 2), triplet (S = 1), and singlet (S = 0) spin states, reflecting differences in metal–ligand interactions. In the quintet state, the Fe–C and Fe–N bonds are notably elongated, indicating a weaker coordination due to the increased spin density localized on the Fe center. Specifically, the Fe–C bond length increases from 1.97 Å in the singlet state to 2.06 Å in the quintet state, while the Fe–N bond length expands from 1.86 Å to 2.13 Å. Additionally, the C–Fe–C bond angle is widest in the quintet state (152.3°), likely due to the steric effects from the distributed spin density.

In this respect, the triplet state exhibits shorter bond lengths (Fe–C = 1.97 Å, Fe–N = 1.87 Å) and a narrower bond angle (163.0°), reflecting stronger metal–ligand interactions. The singlet state is the most compact, with the Fe–C and Fe–N bond lengths closely matching those of the triplet state (Fe–C = 1.97 Å, Fe–N = 1.86 Å), and the singlet state having a slightly narrower bond angle of 163.5°. These observations align well with previous computations for smaller Fe^{2+} complexes [83].

3.3. Electronic Structure and Reactivity Implications

Spin density analysis highlights significant differences in the electronic structure across spin states. In the quintet state, the Fe center exhibits a high spin density (4.00 e$^-$), consistent with its d^6 high-spin electronic configuration [84]. This configuration results in weaker bonding interactions and elongated bonds. The triplet state, with a spin density of 2.17 e$^-$, demonstrates more delocalized electronic interactions, leading to stronger bonding and a more stable geometry. The singlet state, with no unpaired electrons, represents a fully closed-shell configuration, exhibiting the most compact geometry. The geometric and

electronic differences between these spin states are critical for the catalytic cycle. The quintet state, with its higher spin density and weaker bonding, facilitates the initial coordination of N_2O and [9,31–34]. Conversely, the triplet state, with its lower energy and more stable interactions, is better suited for the subsequent steps in the catalytic pathway, such as methane C-H activation.

3.4. Conclusion for [(CNC)Fe^{II}]$^{2+}$ Cation Complexes

The structural and electronic analysis of [(κ^3-CNC)Fe^{II}]$^{2+}$ complexes highlights the interplay between spin states and molecular geometry. The high-spin quintet state provides a reactive intermediate for the initial stages of the catalytic cycle, while the triplet state stabilizes the intermediates in the subsequent steps. These findings underscore the importance of spin-state control in enabling efficient methane activation [85,86].

4. Coordination and Energetics of N_2O to [(κ^3-CNC)Fe^{II}]$^{2+}$ Cation Complex

The coordination of nitrous oxide (N_2O) to the [(κ^3-CNC)Fe^{II}]$^{2+}$ cation complex is a pivotal step in the catalytic cycle, forming the precursor necessary for oxygen atom transfer (OAT). The computational results reveal that the energetic preference between the κ^1-N-bound and κ^1-O-bound configurations depends on both the phase and the spin state of the system.

In the gas phase, the quintet (S = 2) spin state serves as the ground state, favoring the κ^1-O-bound configuration with a Gibbs free energy of −10.2 kcal/mol, compared to 2.0 kcal/mol for the κ^1-N-bound relative to the κ^1-O-bound. Conversely, in tetrahydrofuran (THF), the solvation effects stabilize the κ^1-N-bound intermediate, with a relative Gibbs free energy of 5.0 kcal/mol, compared to 3.7 kcal/mol for the κ^1-O-bound relative to the κ^1-N-bound. This solvent-driven stabilization highlights the critical role of solvation effects in modulating the coordination environment and influencing the spin-state energetics.

Despite the mild endergonic nature of N_2O coordination in the solvent phase (ΔG = 5.0 kcal/mol), the κ^1-N-bound intermediate plays a critical role as the precursor to the high-valent Fe^{IV}=O species formed during OAT. These results underscore the importance of evaluating both gas-phase and solvent-phase energetics to fully understand the catalytic intermediates. Further details of the κ^1-O-bound configuration are provided in the Supporting Information (SI).

4.1. Geometric Features of the Quintet State

The optimized geometry of the κ^1-N-bound quintet (S = 2) state is depicted in Figure 2. In this configuration, nitrous oxide coordinates through its nitrogen atom to the Fe center, resulting in an Fe–N bond length of 2.28 Å and a slightly shortened N–O bond length of 1.15 Å. This shortening suggests that the oxygen atom is pulling the electron density away from the nitrogen atom, increasing the δ^- character of the oxygen and strengthening the N–O bond. The nearly linear Fe–N–N bond angle of 167.9° effectively positions the oxygen atom for transfer to the Fe center during the subsequent oxygen atom transfer (OAT) step [65]. The spin density in this configuration is primarily localized on the Fe center (3.94 e^-), consistent with its high-spin d^6 electronic configuration [84]. This spin localization enhances the Fe–N_2O interaction, allowing for electron donation from the metal center to the N_2O antibonding, which could facilitate subsequent bond cleavage and reorganization during OAT. This geometric and electronic arrangement highlights the critical role of the high-spin quintet state in activating N_2O and positioning the system for efficient catalytic turnover.

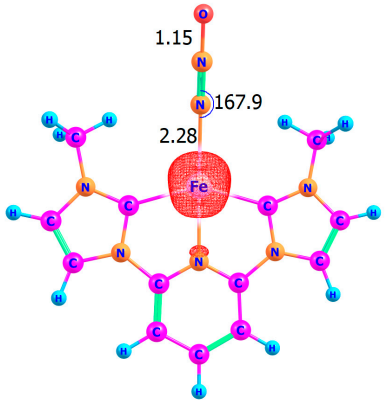

^{5}[NHC-Fe-N$_2$O]

Figure 2. Optimized ground-state geometry of the κ^1-N-bound $[(\kappa^3\text{-CNC})Fe^{II}(N_2O)]^{2+}$ cation complex in the quintet (S = 2) spin state. Bond lengths are given in Å and bond angles in degrees. The near-linear Fe–N–N bond angle (167.9°) facilitates oxygen atom transfer (OAT). The high-spin density (~3.94 e^-) on Fe enhances electron donation to N_2O, promoting N–O bond cleavage and Fe–O bond formation. This step leads to the formation of the Fe^{IV}=O species, a key intermediate in methane activation. The contour value of the spin density plot is 0.020.

4.2. Conclusion for N_2O Coordination

The coordination of N_2O to $[(\kappa^3\text{-CNC})Fe^{II}]^{2+}$ highlights the significance of spin-state effects and molecular geometry in the catalytic process. The exergonic nature of this step in the gas phase, combined with the near-linear Fe–N–N configuration, positions the κ^1-N-bound intermediate as a key precursor for subsequent OAT. Despite the mild energetic nature in the solvent phase, the electronic and structural properties of this intermediate underscore its pivotal role in the catalytic pathway.

5. Oxygen Atom Transfer of N_2O to Form Oxo Fe^{IV} Cation

OAT from nitrous oxide (N_2O) to the $[(\kappa^3\text{-CNC})Fe^{II}]^{2+}$ complex is a critical step in the catalytic cycle, leading to the formation of the high-valent Fe^{IV}=O oxo species. This step involves significant bond reorganization at the transition state (TS) and is identified as the rate-determining step due to its high energy barrier, Figure 3.

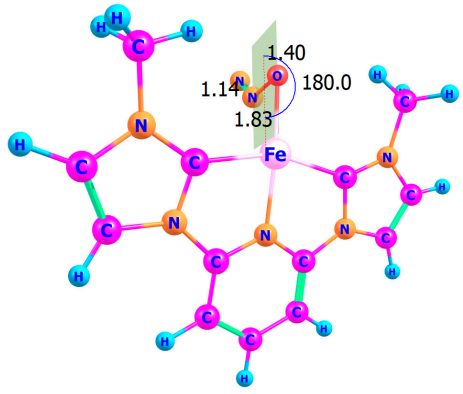

^{3}[OAT-TS1]‡

Figure 3. Optimized geometry of the oxygen atom transfer (OAT) transition state in the triplet (S = 1) spin state, denoted by "‡" for transition state (TS) geometry. Bond lengths are given in Å. The near-linear Fe–O–N–N bond alignment facilitates efficient oxygen atom transfer and N_2 release.

5.1. Geometry and Transition State of OAT

The optimized geometry of the OAT transition state in the triplet (S = 1) spin state reveals key structural features:

- Fe–O Bond Length: 1.83 Å, reflecting the partial formation of the Fe–O bond.
- O–N Bond Length: 1.40 Å, showing significant elongation as the N–O bond undergoes cleavage.
- N–N Bond Length: 1.14 Å, consistent with the release of N_2.
- Fe–O–N–N Bond Angle: 180.0°, indicative of a linear arrangement facilitating efficient oxygen transfer and nitrogen release.

5.2. Spin-State Dependence of OAT

The resulting Fe^{IV}=O intermediate features a strong Fe=O double bond (1.62 Å), as seen in Figure 4, with a pronounced oxo character and partial radical spin density (0.87 e^- on the oxygen atom). This intermediate is pivotal for enabling methane C–H activation in subsequent catalytic steps. The OAT step exhibits a pronounced spin-state dependence, significantly influencing the energetics of the catalytic pathway. Computational results reveal that in the gas phase, the triplet (S = 1) spin state is energetically favored, with a Gibbs free energy barrier of $\Delta G^{\ddagger}$ = 26.3 kcal/mol, compared to $\Delta G^{\ddagger}$ = 36.9 kcal/mol for the quintet (S = 2) spin state, as shown in Scheme 3. This lower barrier highlights the triplet pathway as being the preferred route for initiating the catalytic cycle under gas-phase conditions.

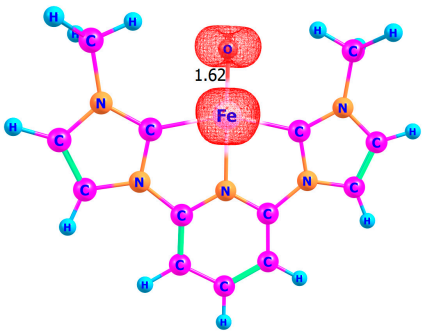

^{5}[OXO/OXYL]

Figure 4. Optimized ground state geometry and spin density distribution of the Fe^{IV}=O complex in the quintet (S = 2) spin state. Bond lengths are given in Å, and spin density values (e^-) are shown on the Fe center and O atom. The oxyl radical character of the oxygen atom (~0.87 e^-) and the high-spin Fe center (~3.16 e^-) make this complex a highly reactive intermediate for methane activation. The contour value of the spin density plot is 0.020.

The reduced barrier for the triplet state arises from its ability to better stabilize the transition state geometry through enhanced electronic reorganization during the bond-breaking and bond-forming processes. In contrast, the higher barrier for the quintet state can be attributed to the increased spin density localized on the Fe center, which raises the energetic cost of rearranging bonding interactions during OAT.

These findings underscore the critical role of spin-state dynamics in determining reaction energetics. By favoring the triplet state for the initial activation step, the catalytic system achieves a more accessible pathway for the OAT process, setting the stage for subsequent methane functionalization.

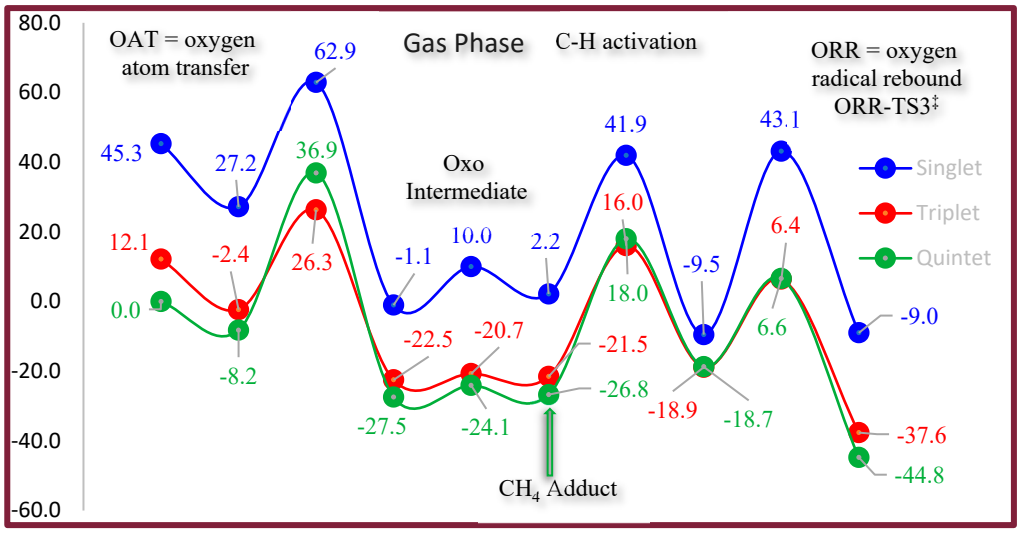

Scheme 3. Free energy profile for the catalytic cycle of methane activation by the Fe^{IV}=O complex in the gas phase. The energy barriers for the OAT, HAA, and ORR steps are shown for the singlet (**blue**), triplet (red), and quintet (**green**) spin states. Energies are reported as Gibbs free energies (ΔG) in kcal/mol, with the triplet and quintet spin states exhibiting competitive pathways, while the singlet state remains energetically less favorable. The key transition states and intermediates are highlighted along with the reaction coordinate.

5.3. Solvent Effects and Alternative Solvent Recommendations

In the THF solvent phase, the Gibbs free energy barrier for the OAT step increases significantly, rising to $\Delta G^{\ddagger}$ = 53.2 kcal/mol, as shown in Scheme 4. This substantial increase indicates that solvation effects destabilize the Fe complex during this step. The destabilization likely stems from THF's solvation of the reactants, which preferentially lowers the energy of the initial state relative to the transition state, resulting in higher overall free energy barriers.

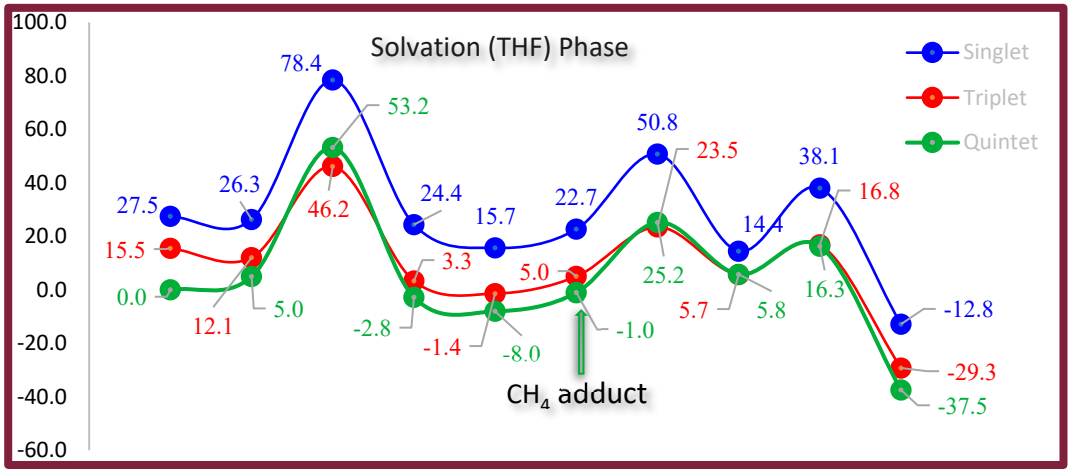

Scheme 4. Free energy profile for the catalytic cycle of methane activation by the Fe^{IV}=O complex in the solvation (THF) phase. The energy barriers for the OAT, HAA, and ORR steps are shown for the singlet (**blue**), triplet (red), and quintet (**green**) spin states. Energies are reported as Gibbs free energies (ΔG) in kcal/mol, with the triplet and quintet spin states exhibiting competitive pathways, while the singlet state remains energetically less favorable. The key transition states and intermediates are highlighted along with the reaction coordinate.

While THF is commonly employed due to its moderate polarity and compatibility with transition metal complexes, its impact on the energetics of critical steps such as OAT

and HAA suggests the need to explore alternative solvents. Optimizing the solvation environment could mitigate these destabilizing effects and enhance catalytic efficiency.

5.4. Alternative Solvents

To address the limitations observed with THF, several alternative solvents are proposed:

1. Polar Aprotic Solvents:
   - Acetonitrile (CH_3CN): A highly polar, non-coordinating solvent that minimizes interactions with the Fe center while providing the strong stabilization of polar intermediates and transition states. Previous studies have shown that acetonitrile improves reaction kinetics by facilitating charge separation and stabilizing high-valent metal–oxo species [87].
   - Dimethylformamide (DMF): A high-polarity solvent that enhances the stability of charged species but may introduce undesired ligand competition with the Fe center. Studies indicate that DMF can reduce transition state energy barriers for oxidative transformations in Fe-based catalysis.
2. Dimethyl Sulfoxide (DMSO):
   - DMSO effectively stabilizes charged intermediates due to its high dielectric constant. However, its coordinating nature may lead to direct interactions with Fe, potentially altering the catalytic pathways [87]. Some Fe-based systems show enhanced selectivity in DMSO, while others experience competitive ligand effects [56].
3. Moderate Polarity Solvents:
   - Dichloromethane (DCM) and ethyl acetate (EtOAc): These solvents provide a balance between polarity and inertness, stabilizing key intermediates without significant coordination with the Fe center. Their ability to influence reaction rates and selectivity has been demonstrated in transition-metal-catalyzed oxidation reactions [58].
4. Nonpolar Solvents:
   - Toluene and other nonpolar solvents may reduce solvation effects and lower transition state energies, particularly in systems where polar solvents over-stabilize reactants. Previous research suggests that nonpolar solvents improve Fe-catalyzed hydrocarbon oxidations by favoring reactive high-spin states [67].
   - Co-solvent Strategies: Combining nonpolar solvents with small amounts of polar co-solvents could fine-tune the solvation effects, optimizing catalytic performance [69].

5.5. Conclusion of OAT Mechanism

The choice of solvent significantly influences the energetics of the reaction cycle, particularly for steps like OAT. Polar aprotic solvents such as acetonitrile and moderately polar solvents like DCM offer promising alternatives for mitigating the destabilizing effects observed in THF. Nonpolar environments, potentially those augmented with polar co-solvents, also present viable options. Selecting the optimal solvent is critical for minimizing free energy barriers and maximizing the overall catalytic efficiency.

6. Structure and Properties of the Fe^{IV}=O Complex

The Fe^{IV}=O oxo complex, formed during the OAT step, serves as a key reactive intermediate in the catalytic cycle. This species exhibits distinct geometric and electronic properties that are crucial for facilitating subsequent methane C–H activation via hydrogen atom abstraction (HAA).

Geometric Characterization of Oxo/Oxyl Complex

The optimized geometry of the Fe^{IV}=O complex reveals key structural characteristics, as summarized below:

- Fe=O Bond Length: 1.62 Å, indicative of a strong double bond with significant oxo character.
- CNC Ligand Coordination: The CNC ligand maintains a distorted square planar geometry around the Fe center, with the oxo ligand occupying an axial position.
- Spin-State Configurations: The geometric variations between the triplet (S = 1) and quintet (S = 2) states highlight the influence of the spin state on bond lengths and the coordination environment.

7. Spin-State Energetics

The Fe^{IV}=O complex demonstrates spin-state-dependent stability:

1. Quintet (S = 2) State: The quintet spin state is the ground-state configuration for the Fe^{IV}=O species. The high spin density (3.16 e^- on Fe and 0.87 e^- on O) reflects the distribution of unpaired electrons, which enhances the oxyl radical character of the oxygen atom. This configuration is stabilized by the strong σ-donation from the oxo group and π-backbonding interactions with the CNC ligand.
2. Triplet (S = 1) State: While the triplet state plays a critical role during the OAT step, it lies higher in terms of energy (by ~3–7 kcal/mol depending on the environment phase) compared to the quintet state for the Fe^{IV}=O species. This energy gap facilitates a spin flip to the quintet state after OAT, enabling the complex to adopt its thermodynamically preferred configuration.

7.1. Electronic Structure

The electronic structure of the Fe^{IV}=O complex is characterized by significant oxo radical character, as evidenced by the spin density distribution:

- Iron Center (Fe): Spin density of 3.17 e^- in the quintet state, consistent with its d^4 configuration.
- Oxo Ligand (O): Partial spin density of 0.87 e^-, indicative of an oxyl radical. This feature is critical for activating methane via HAA.

The strong Fe=O bond and oxyl radical nature enhance the reactivity of the complex, making it a potent oxidant capable of cleaving the strong C–H bond in methane.

7.2. Reactivity Implications

The Fe^{IV}=O oxo species is uniquely suited for methane activation due to its electronic and spin properties:

1. Oxo Radical Rebound: The oxyl radical character facilitates rapid rebound with the methyl radical during the oxygen radical rebound (ORR) step, ensuring the efficient formation of methanol.
2. Hydrogen Atom Abstraction (HAA): The Fe^{IV}=O species initiates HAA by abstracting a hydrogen atom from methane, driven by its strong oxidizing potential and spin-state reactivity.

7.3. Conclusion Oxo/Oxyl Characterization

The Fe^{IV}=O oxo complex is a critical intermediate in the catalytic cycle, with its structure and spin-state properties directly influencing its reactivity. The ground-state quintet configuration, stabilized by strong Fe=O bonding and the oxo radical character, sets the stage for efficient methane C–H activation. The spin flip from the triplet state

after OAT further underscores the dynamic role of spin-state transitions in enabling the catalytic mechanism.

8. Methane C–H Activation by Oxo/Oxyl Cation Complex

Methane C–H activation by the Fe^{IV}=O oxo cation complex involves two pivotal steps: HAA and ORR, culminating in the formation of methanol. The catalytic efficiency stems from the electronic and geometric properties of the Fe^{IV}=O intermediate, with spin-state dynamics playing a significant role. Figures 5 and 6 illustrate the transition state (TS) geometries for HAA and ORR, while Table 2 and Schemes 3 and 4 summarize the energetics and free energy profiles.

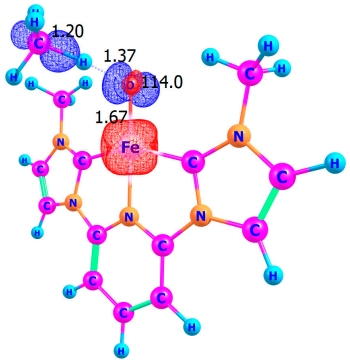

^{3}[HAA-TS2]‡

Figure 5. Optimized transition state geometry for HAA by the Fe^{IV}=O oxo complex in the triplet (S = 1) spin state, denoted by "‡" for transition state (TS) geometry. Bond lengths are given in Å, and bond angles in degrees. Red = positive spin density and blue = negative spin density. The contour value of the spin density plot is 0.020.

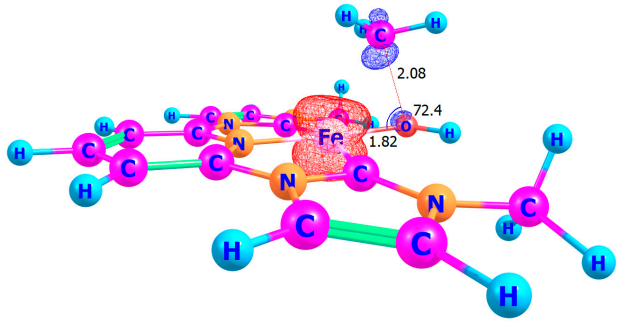

^{3}[ORR-TS3]‡

Figure 6. Optimized transition state geometries for ORR by the Fe^{III}–OH intermediate in the triplet (S = 1) spin state, denoted by "‡" for transition state (TS) geometry. Bond lengths are given in Å, and bond angles in degrees. Red = positive spin density and blue = negative spin density. The contour value of the spin density plot is 0.020.

Table 2. Geometric and energetic parameters for HAA and ORR by the Fe^{IV}=O complex in methane activation.

Parameter	Gas Phase (Triplet)	Gas Phase (Quintet)	THF Solvent (Triplet)	THF Solvent (Quintet)
$\Delta G^{\ddagger}$ HAA (kcal/mol)	16.0	18.0	23.5	25.2
$\Delta G^{\ddagger}$ ORR (kcal/mol)	6.4	6.6	16.8	16.3
Fe–O (HAA, Å)	1.67	1.72	1.67	1.72
O–H (HAA, Å)	1.37	1.22	1.37	1.22
C–H (HAA, Å)	1.20	1.33	1.20	1.33
Fe–O–H (HAA, °)	114.0	94.1	114.0	94.1
Fe–O (ORR, Å)	1.82	1.82	1.80	1.82
O–C (ORR, Å)	2.08	2.17	2.08	2.17
Fe–O–C (ORR, °)	74.2	71.4	74.2	71.4

8.1. Hydrogen Atom Abstraction (HAA)

The HAA step is initiated when the oxygen atom of the Fe^{IV}=O complex abstracts a hydrogen atom from methane. This process involves the formation of an O–H bond and the elongation of the C–H bond.

8.2. Geometric Descriptions of Figures 5 and 6

The transition state (TS) geometries for HAA by the Fe^{IV}=O complex reveal distinct structural features for the quintet (S = 2) and triplet (S = 1) spin states, highlighting their different reactivity profiles. In the quintet state, the Fe–O bond length is slightly elongated at 1.72 Å, reflecting a partially formed O–H bond (1.22 Å) and a C–H bond stretched to 1.33 Å. The Fe–O–H bond angle of 94.1° indicates a compact geometry that facilitates interaction between the Fe^{IV}=O center and the incoming hydrogen atom. In contrast, the triplet state exhibits a shorter Fe–O bond length of 1.67 Å, with a more extended O–H bond of 1.37 Å and a slightly compressed C–H bond of 1.20 Å. The Fe–O–H bond angle in the triplet state is 114.0°, suggesting a more open transition state geometry that may enhance the accessibility of the substrate. These differences underscore the spin-dependent nature of the HAA step, with the triplet state favoring tighter bonding at the oxygen center and the quintet state enabling a more compact and symmetric transition state geometry.

8.3. The Quintet and Triplet State Spin Densities

The spin density distribution provides critical insights into the electronic structure of the Fe^{IV}=O complex and its reactivity during hydrogen atom abstraction (HAA). In the quintet state (S = 2), the Fe center retains a spin density of 2.91 e^{-}, while the oxygen atom exhibits a spin density of 0.67 e^{-}. This distribution reflects the partial transfer of electron density during HAA, with the oxygen atom displaying moderate oxyl radical character. In contrast, the triplet state (S = 1) shows a slightly lower Fe spin density of 2.87 e^{-}, accompanied by a reduced oxygen spin density of 0.32 e^{-}. This stronger oxyl radical character in the triplet state highlights its enhanced ability to facilitate the bond-breaking and bond-forming processes, making it more reactive compared to the quintet state. The differences in spin density distributions underscore the critical role of spin-state dynamics in determining the reactivity and efficiency of the catalytic cycle. The higher oxyl radical character in the triplet state aligns with its lower energy barrier for HAA, further emphasizing the triplet state as the preferred pathway for methane activation.

8.4. Energetic Barrier of Figure 5

In the gas phase, the triplet state exhibits a lower free energy barrier than the quintet state, with barriers of 16.0 and 18.0 kcal/mol, respectively. In THF, the barriers increase to 23.5 and 25.2 kcal/mol for the triplet and quintet states, respectively. These data indicate that HAA is energetically more favorable in the gas phase than in the solvent phase, regardless of the spin state.

A notable trend observed is the significantly higher transition state (TS) energies in THF compared to the gas phase. This difference arises from the differential stabilization provided by the solvent. As a polar medium, THF stabilizes the reactants, particularly the Fe^{IV}=O complex, through favorable solvation interactions with its polarized nature. However, the transition states, characterized by strained geometries and substantial charge redistribution, do not benefit equally from these solvation effects. Consequently, the relative Gibbs free energy barriers for both HAA and ORR increase in the solvated phase. This trend underscores the nuanced role of the solvent environment in modulating the energetics and mechanisms of catalytic pathways, emphasizing the importance of solvent selection in optimizing reaction conditions.

9. Oxygen Radical Rebound (ORR)

Following HAA, the methyl radical recombines with the hydroxyl group of the Fe^{III}–OH intermediate, completing the catalytic cycle by forming methanol.

9.1. Geometric Features of ORR TS Structure

The transition state (TS) geometries for ORR reveal distinct features for the quintet (S = 2) and triplet (S = 1) spin states, reflecting their differing mechanistic pathways. In the quintet state, the Fe–O bond length is 1.82 Å, indicating the partial dissociation of the Fe–O bond as the O–C bond forms with a length of 2.17 Å. The Fe–O–C bond angle of 71.4° suggests a compact arrangement, facilitating the efficient recombination of the hydroxyl group with the methyl radical to form methanol. Conversely, the triplet state also exhibits an Fe–O bond length of 1.82 Å, but a slightly shorter O–C bond of 2.08 Å, indicative of a more flexible transition state. The Fe–O–C bond angle in the triplet state is 72.4°, reflecting a slightly more open geometry that may enhance the orbital alignment for the rebound step. These structural differences underscore the spin-state dependence of the ORR mechanism, with the quintet state favoring a compact transition state geometry, while the triplet state exhibits enhanced flexibility.

9.2. Spin Densities of the ORR TS Structure

In the quintet state, the Fe center exhibits a spin density of 4.01 e^-, while the oxygen atom displays a negligible spin density, indicating electron pairing as the O–C bond forms during methanol generation. In the triplet state, the Fe center's spin density decreases to 0.14 e^-, and the oxygen atom's spin density is -0.50 e^-, further confirming its role as a reactant in the rebound step and its contribution to stabilizing the methanol product.

9.3. Energetic Barrier of Figure 6

The ORR step, where the methyl radical recombines with the hydroxyl group of the Fe^{III}–OH intermediate to form methanol, is characterized by moderate Gibbs free energy barriers. In the gas phase, the free energy barrier ($\Delta G^{\ddagger}$) for the triplet (S = 1) state is 6.4 kcal/mol, while the quintet (S = 2) state exhibits a slightly higher barrier of 6.6 kcal/mol. These values indicate that both spin states are energetically favorable for this step under gas-phase conditions. In the THF solvent phase, the free energy barriers increase significantly due to solvation effects. The triplet state shows a barrier of 16.8 kcal/mol, while the quintet

state has a barrier of 16.3 kcal/mol. The smaller energy difference between the two spin states in the solvent phase suggests a reduced spin-state dependence during ORR when solvation is considered. These barriers remain accessible under typical catalytic conditions, emphasizing the feasibility of methanol formation via the ORR mechanism.

9.4. Conclusions

Methane activation by the Fe^{IV}=O oxo complex involves efficient HAA and ORR. The triplet (S = 1) state generally provides lower barriers for HAA, while ORR exhibits reduced spin-state dependence. These results underscore the catalytic potential of CNC-ligated iron complexes for selective methane functionalization.

10. Summary and Conclusions

This study employed DFT to investigate the catalytic activation of methane using CNC-ligated iron complexes, with nitrous oxide as the oxidant. The computational analysis elucidated the mechanistic steps of OAT, HAA, and ORR, with a particular emphasis on spin-state dynamics and solvent effects.

Our key findings include the following:

- The CNC-ligated iron complexes effectively stabilize high-valent Fe intermediates, facilitating methane C–H activation under mild conditions.
- The triplet (S = 1) and quintet (S = 2) spin states play distinct but complementary roles in the catalytic cycle, with intersystem crossing (ISC) enhancing reactivity.
- The OAT step is the rate-determining step, with the energy barriers influenced by solvation effects and the electronic structure.
- The Fe^{IV}=O intermediate exhibits significant oxyl radical character, enabling efficient methane C–H activation via HAA.
- The ORR step proceeds with moderate energy barriers, ensuring methanol formation is feasible.
- Solvent choice significantly impacts reaction energetics, with alternative solvents such as acetonitrile or DMSO potentially improving catalytic efficiency [54,58].

Beyond mechanistic insights, this work highlights the dual environmental benefits of CNC-ligated iron complexes, as follows: enabling methane functionalization while reducing atmospheric nitrous oxide, a potent greenhouse gas. These findings establish a foundation for future experimental validation, catalyst optimization, and the exploration of broader hydrocarbon applications, paving the way for more efficient and sustainable methane oxidation processes.

11. Prospectus

The findings of this study open several avenues for future research and practical development:

1. Experimental Validation: The computationally derived mechanisms and spin-state energetics provide a foundation for experimental efforts to synthesize and characterize CNC-ligated iron complexes under conditions analogous to those modeled computationally.
2. Ligand Optimization: Future work could explore alternative CNC ligand scaffolds or substitutions to enhance stability, selectivity, and catalytic turnover, especially for systems involving polar or nonpolar solvent environments.
3. Solvent Engineering: The demonstrated impact of solvation on OAT and methane activation highlights the need for further exploration of mixed solvent systems or highly nonpolar environments to optimize solvation-induced energy barriers.
4. Broader Substrate Scope: Beyond methane, this catalytic approach could be extended to other hydrocarbons or small molecules, broadening its applicability in chemical synthesis.

5. Industrial Scale-Up: Developing scalable processes for methanol production using N_2O as an oxidant could reduce the reliance on conventional, energy-intensive methods like steam methane reforming, aligning with global sustainability goals.

These prospects underscore the transformative potential of CNC-ligated iron catalysts in advancing methane utilization and greenhouse gas mitigation.

In summary, this work highlights CNC-ligated iron catalysts as a compelling solution to critical environmental and industrial challenges, paving the way for more sustainable and efficient chemical transformations.

Supplementary Materials: The following supporting information can be downloaded at: https://www.mdpi.com/article/10.3390/methane4010006/s1. The Cartesian coordinates of all calculated species, along with their spin multiplicities and full citation details, are provided.

Funding: This work was supported in part by Texas Southern University (TSU) High Performance Computing Center (https://coset.tsu.edu/hpcc/, Grant PHY-1126251); Texas Southern University Department of Chemistry; and The Center for Computational Catalysis Research (3CR).

Institutional Review Board Statement: Not applicable.

Informed Consent Statement: Not applicable.

Data Availability Statement: Data are contained within the article.

Conflicts of Interest: The authors declare no competing financial interests.

References

1. Zhou, J.; Xu, Y.; Zhou, X.; Gong, J.; Yin, Y.; Zheng, H.; Guo, H. Direct Oxidation of Methane to Hydrogen Peroxide and Organic Oxygenates in a Double Dielectric Plasma Reactor. *ChemSusChem* **2011**, *4*, 1095. [CrossRef] [PubMed]
2. Zimmermann, T.; Soorholtz, M.; Bilke, M.; Schüth, F. Selective methane oxidation catalyzed by platinum salts in oleum at turnover frequencies of large-scale industrial processes. *J. Am. Chem. Soc.* **2016**, *138*, 12395. [CrossRef]
3. Zerella, M.; Mukhopadhyay, S.; Bell, A.T. Direct oxidation of methane to acetic acid catalyzed by Pd^{2+} and Cu^{2+} in the presence of molecular oxygen. *Chem. Commun.* **2004**, 1948–1949. [CrossRef]
4. Zerella, M.; Kahros, A.; Bell, A.T. Methane oxidation to acetic acid catalyzed by Pd^{2+} cations in the presence of oxygen. *J. Catal.* **2006**, *237*, 111. [CrossRef]
5. Yang, H.; Hu, C.; Qin, S. Theoretical study on the reaction mechanism of CH_4 with CaO. *Chem. Phys.* **2006**, *330*, 343–348. [CrossRef]
6. Yamanaka, I.; Soma, M.; Oisuka, K. Oxidation of methane to methanol with oxygen catalysed by europium trichloride at room temperature. *J. Chem. Soc. Chem. Commun.* **1995**, 2235–2236. [CrossRef]
7. Yuan, J.; Wang, L.; Wang, Y. Direct Oxidation of Methane to a Methanol Derivative Using Molecular Oxygen. *Ind. Eng. Chem. Res.* **2011**, *50*, 6513. [CrossRef]
8. Prince, B.M. A computational DFT study of methane CH and ammine NH activations by group 9 N-pyrrolyl complexes. *Comput. Theor. Chem.* **2019**, *1162*, 112503. [CrossRef]
9. Prince, B.M.; Gunnoe, T.B.; Cundari, T.R. Oxy-functionalization of Group 9 and 10 transition metal methyl ligands: Use of pyridine-based hemi-labile ligands. *Dalton Trans.* **2014**, *43*, 7608–7614. [CrossRef]
10. Prince, B.M.; Cundari, T.R.; Tymczak, C.J. DFT Study of the Reaction of a Two-Coordinate Iron(II) Dialkyl Complex with Molecular Oxygen. *J. Phys. Chem. A* **2014**, *118*, 11056–11061. [CrossRef]
11. Prince, B.M.; Cundari, T.R. C–H Bond Activation of Methane by PtII–N-Heterocyclic Carbene Complexes. The Importance of Having the Ligands in the Right Place at the Right Time. *Organometallics* **2012**, *31*, 1042–1048. [CrossRef]
12. Prince, B.M.; Cundari, T.R. Methane C-H Bond Activation by "Naked" Alkali Metal Imidyl and Alkaline Earth Metal Imide Complexes. The Role of Ligand Spin and Nucleophilicity. *J. Phys. Chem. A* **2013**, *117*, 9245–9251. [CrossRef] [PubMed]
13. Sakaki, S.; Biswas, B.; Sugimoto, M. Oxidative addition of a C–H σ bond to $M(PH_3)_2$ (M=Pd or Pt). An ab initio molecular orbital study on the chelate phosphine effect. *J. Chem. Soc. Dalton Trans.* **1997**, 803–810. [CrossRef]
14. Jursic, B.S.; Timberlake, J.W.; Engel, P.S. Computation of bond dissociation energies of substituted methanes with density functional theory. *Tetrahedron Lett.* **1996**, *37*, 6473–6474. [CrossRef]
15. Blanksby, S.J.; Ellison, G.B. Bond Dissociation Energies of Organic Molecules. *Acc. Chem. Res.* **2003**, *36*, 255–263. [CrossRef]

16. Gunsalus, N.J.; Koppaka, A.; Park, S.H.; Bischof, S.M.; Hashiguchi, B.G.; Periana, R.A. Homogeneous Functionalization of Methane. *Chem. Rev.* **2017**, *117*, 8521–8573. [CrossRef] [PubMed]
17. Sobalík, Z.; Tabor, E.; Nováková, J.; Sathu, N.K.; Závěta, K. Role of active oxygen and NO_x species in N_2O decomposition over Fe-ferrierite. *J. Catal.* **2012**, *289*, 164–170. [CrossRef]
18. Meng, X.; Cui, X.; Rajan, N.P.; Yu, L.; Deng, D.; Bao, X. Direct Methane Conversion under Mild Condition by Thermo-, Electro-, or Photocatalysis. *Chem* **2019**, *5*, 2296–2325. [CrossRef]
19. Paul, A.; Musgrave, C.B. A Detailed Theoretical Study of the Mechanism and Energetics of Methane to Methanol Conversion by Cisplatin and Catalytica. *Organometallics* **2007**, *26*, 793–809. [CrossRef]
20. Fifth Assessment Report—IPCC. Available online: https://www.ipcc.ch/assessment-report/ar5/ (accessed on 31 July 2024).
21. Special Report on the Ocean and Cryosphere in a Changing Climate. Available online: https://www.ipcc.ch/srocc/ (accessed on 31 July 2024).
22. Sixth Assessment Report—IPCC. Available online: https://www.ipcc.ch/assessment-report/ar6/ (accessed on 31 July 2024).
23. Bahrami, M.; Pourfayaz, F.; Kasaeian, A. Low global warming potential (GWP) working fluids (WFs) for Organic Rankine Cycle (ORC) applications. *Energy Rep.* **2022**, *8*, 2976–2988. [CrossRef]
24. Danny Harvey, L.D. A guide to global warming potentials (GWPs). *Energy Policy* **1993**, *21*, 24–34. [CrossRef]
25. Sanz-Cobena, A.; Sánchez-Martín, L.; García-Torres, L.; Vallejo, A. Gaseous emissions of N_2O and NO and NO_3^- leaching from urea applied with urease and nitrification inhibitors to a maize (*Zea mays*) crop. *Agric. Ecosyst. Environ.* **2012**, *149*, 64–73. [CrossRef]
26. Wang, J.; Xiong, Z.; Yan, X. Fertilizer-induced emission factors and background emissions of N_2O from vegetable fields in China. *Atmos. Environ.* **2011**, *45*, 6923–6929. [CrossRef]
27. Tierling, J. *The Effects of Different Mineral Nitrogen Fertilizer Forms on N_2O Emissions from Arable Soils Under Aerobic Conditions*; Cuvillier Verlag: Göttingen, Germany, 2017.
28. Zhang, J.-S.; Zhang, F.-P.; Yang, J.-H.; Wang, J.-P.; Cai, M.-L.; Li, C.-F.; Cao, C.-G. Emissions of N_2O and NH_3, and nitrogen leaching from direct seeded rice under different tillage practices in central China. *Agric. Ecosyst. Environ.* **2011**, *140*, 164–173.
29. Jurado, A.; Borges, A.; Brouyère, S. Dynamics and emissions of N_2O in groundwater: A review. *Sci. Total Environ.* **2017**, *584–585*, 207–218. [CrossRef]
30. Olah, G.A.; Goeppert, A.; Prakash, G.K.S. *Beyond Oil and Gas the Methanol Economy*; Wiley-VCH: Weinheim, Germany, 2018.
31. Nam, W. High-Valent Iron(IV)–Oxo Complexes of Heme and Non-Heme Ligands in Oxygenation Reactions. *Acc. Chem. Res.* **2007**, *40*, 522–531. [CrossRef]
32. Matsunaga, P.T.; Mavropoulos, J.C.; Hillhouse, G.L. Oxygen-atom transfer from nitrous oxide (N=N=O) to nickel alkyls. Syntheses and reactions of nickel(II) alkoxides. *Polyhedron* **1995**, *14*, 175–185. [CrossRef]
33. Mei, J.; Carsch, K.M.; Freitag, C.R.; Gunnoe, T.B.; Cundari, T.R. Variable Pathways for Oxygen Atom Insertion into Metal-Carbon Bonds: The Case of $Cp^*W(O)_2(CH_2SiMe_3)$. *J. Am. Chem. Soc.* **2013**, *135*, 424–435. [CrossRef]
34. Matsunaga, P.T.; Hillhouse, G.L.; Rheingold, A.L. Oxygen-atom transfer from nitrous oxide to a nickel metallacycle. Synthesis, structure, and reactions of [cyclic] (2,2′-bipyridine)Ni(OCH2CH2CH2CH2). *J. Am. Chem. Soc.* **1993**, *115*, 2075–2077. [CrossRef]
35. Burch, R.; Daniells, S.T.; Breen, J.P.; Hu, P. A combined transient and computational study of the dissociation of N_2O on platinum catalysts. *J. Catal.* **2004**, *224*, 252–260. [CrossRef]
36. Martínez, A.; Goursot, A.; Coq, B.; Delahay, G. Theoretical Study of the Dissociation of N_2O in a Transition Metal Ion-Catalyzed Reaction. *J. Phys. Chem. B* **2004**, *108*, 8823–8829. [CrossRef]
37. Dibeler, V.H. N_2O Bond Dissociation Energy by Photon Impact. *J. Chem. Phys.* **1967**, *47*, 2191–2192. [CrossRef]
38. Danopoulos, A.; Pugh, D.; Smith, H.; Saßmannshausen, J. Structural and Reactivity Studies of "Pincer" Pyridine Dicarbene Complexes of Fe0: Experimental and Computational Comparison of the Phosphine and NHC Donors. *Chem. A Eur. J.* **2009**, *15*, 5491–5502. [CrossRef]
39. Darmon, J.M.; Yu, R.P.; Semproni, S.P.; Turner, Z.R.; Stieber, S.C.; DeBeer, S.; Chirik, P.J. Electronic Structure Determination of Pyridine N-Heterocyclic Carbene Iron Dinitrogen Complexes and Neutral Ligand Derivatives. *Organometallics* **2014**, *33*, 5423–5433. [CrossRef]
40. Scott, N.M.; Stevens, E.D.; Dorta, R.; Costabile, C.; Cavallo, L.; Hoff, C.D.; Nolan, S.P. Steric and Electronic Properties of N-Heterocyclic Carbenes (NHC): A Detailed Study on Their Interaction with $Ni(CO)_4$. *J. Am. Chem. Soc.* **2005**, *127*, 2485–2495.
41. Rosen, E.L.; Varnado, C.D.; Tennyson, A.G.; Khramov, D.M.; Kamplain, J.W.; Sung, D.H.; Cresswell, P.T.; Lynch, V.M.; Bielawski, C.W. Redox-Active N-Heterocyclic Carbenes: Design, Synthesis, and Evaluation of Their Electronic Properties. *Organometallics* **2009**, *28*, 6695–6706. [CrossRef]
42. Peìrez, P.J.; DiÌaz-Requejo, M.M.; Nolan, S.P. *N-Heterocyclic Carbenes in Synthesis*; John Wiley & Sons: Hoboken, NJ, USA, 2006.
43. Muehlhofer, M.; Strassner, T.; Herrmann, W.A. New Catalyst Systems for the Catalytic Conversion of Methane into Methanol. *Angew. Chem. Int. Ed.* **2002**, *41*, 1745–1747. [CrossRef]

44. Kiernicki, J.J.; Zeller, M.; Szymczak, N.K. Requirements for Lewis Acid-Mediated Capture and N–N Bond Cleavage of Hydrazine at Iron. *Inorg. Chem.* **2019**, *58*, 1147–1154. [CrossRef]
45. Zimmer, P.; Burkhardt, L.; Friedrich, A.; Steube, J.; Neuba, A.; Schepper, R.; Müller, P.; Flörke, U.; Huber, M.; Lochbrunner, S.; et al. The Connection between NHC Ligand Count and Photophysical Properties in Fe(II) Photosensitizers: An Experimental Study. *Inorg. Chem.* **2018**, *57*, 360–373. [CrossRef] [PubMed]
46. Danopoulos, A.A.; Wright, J.A.; Motherwell, W.B.; Ellwood, S. N-Heterocyclic "Pincer" Dicarbene Complexes of Cobalt(I), Cobalt(II), and Cobalt(III). *Organometallics* **2004**, *23*, 4807. [CrossRef]
47. Arduengo, A.J.; Gamper, S.F.; Calabrese, J.C.; Davidson, F. Low-Coordinate Carbene Complexes of Nickel(0) and Platinum(0). *J. Am. Chem. Soc.* **1994**, *116*, 4391–4394. [CrossRef]
48. Arduengo, A.J. Looking for Stable Carbenes: The Difficulty in Starting Anew. *Acc. Chem. Res.* **1999**, *32*, 913–921. [CrossRef]
49. Arduengo, A.J.; Harlow, R.L.; Kline, M. A stable crystalline carbene. *J. Am. Chem. Soc.* **1991**, *113*, 361–363. [CrossRef]
50. Zimmer, P.; Müller, P.; Burkhardt, L.; Schepper, R.; Neuba, A.; Steube, J.; Dietrich, F.; Flörke, U.; Mangold, S.; Gerhards, M. N-Heterocyclic Carbene Complexes of Iron as Photosensitizers for Light-Induced Water Reduction. *Eur. J. Inorg. Chem.* **2017**, *2017*, 1504–1509. [CrossRef]
51. Danopoulos, A.A.; Simler, T.; Braunstein, P. N-Heterocyclic Carbene Complexes of Copper, Nickel, and Cobalt. *Chem. Rev.* **2019**, *119*, 3730–3961. [CrossRef] [PubMed]
52. Dröge, T.; Glorius, F. The Measure of All Rings—N-Heterocyclic Carbenes. *Angew. Chem. Int. Ed.* **2010**, *49*, 6940–6952. [CrossRef] [PubMed]
53. Dalton, T.; Faber, T.; Glorius, F. C–H Activation: Toward Sustainability and Applications. *ACS Cent. Sci.* **2021**, *7*, 245–261. [CrossRef]
54. Groves, J.T. High-valent iron in chemical and biological oxidations. *J. Inorg. Biochem.* **2006**, *100*, 434–447. [CrossRef]
55. Moody, P.C.E.; Raven, E.L. The Nature and Reactivity of Ferryl Heme in Compounds I and II. *Acc. Chem. Res.* **2018**, *51*, 427–435. [CrossRef]
56. Que, L.; Tolman, W.B. Biologically inspired oxidation catalysis. *Nature* **2008**, *455*, 333–340. [CrossRef]
57. McDonald, A.R.; Que, L. High-valent nonheme iron-oxo complexes: Synthesis, structure, and spectroscopy. *Coord. Chem. Rev.* **2013**, *257*, 414–428. [CrossRef]
58. Krebs, C.; Galonić Fujimori, D.; Walsh, C.T.; Bollinger, J.M. Non-Heme Fe(IV)–Oxo Intermediates. *Acc. Chem. Res.* **2007**, *40*, 484–492. [CrossRef] [PubMed]
59. Wang, Y.; Olankitwanit, A.; Rajca, S.; Rajca, A. Intramolecular Hydrogen Atom Transfer in Aminyl Radical at Room Temperature with Large Kinetic Isotope Effect. *J. Am. Chem. Soc.* **2017**, *139*, 7144–7147. [CrossRef]
60. Valgimigli, L.; Banks, J.T.; Ingold, K.U.; Lusztyk, J. Kinetic Solvent Effects on Hydroxylic Hydrogen Atom Abstractions Are Independent of the Nature of the Abstracting Radical. Two Extreme Tests Using Vitamin E and Phenol. *J. Am. Chem. Soc.* **1995**, *117*, 9966–9971. [CrossRef]
61. Seal, P.; Oyedepo, G.; Truhlar, D.G. Kinetics of the Hydrogen Atom Abstraction Reactions from 1-Butanol by Hydroxyl Radical: Theory Matches Experiment and More. *J. Phys. Chem. A* **2013**, *117*, 275. [CrossRef] [PubMed]
62. Renaud, P.; Beaufils, F.; Feray, L.; Schenk, K. Diastereoselective Radical-Mediated Hydrogen-Atom Abstraction. *Angew. Chem. Int. Ed.* **2003**, *42*, 4230–4233. [CrossRef] [PubMed]
63. Neidig, M.L.; Decker, A.; Choroba, O.W.; Huang, F.; Kavana, M.; Moran, G.R.; Spencer, J.B.; Solomon, E.I. Spectroscopic and electronic structure studies of aromatic electrophilic attack and hydrogen-atom abstraction by non-heme iron enzymes. *Proc. Natl. Acad. Sci. USA* **2006**, *103*, 12966. [CrossRef]
64. Mayer, J.M. Hydrogen Atom Abstraction by Metal−Oxo Complexes: Understanding the Analogy with Organic Radical Reactions. *Acc. Chem. Res.* **1998**, *31*, 441–450. [CrossRef]
65. Mai, B.K.; Kim, Y. Is It Fe(III)-Oxyl Radical That Abstracts Hydrogen in the C–H Activation of TauD? A Theoretical Study Based on the DFT Potential Energy Surfaces. *Inorg. Chem.* **2016**, *55*, 3844–3852. [CrossRef]
66. Shubin, A.A.; Ruzankin, S.P.; Zilberberg, I.L.; Parmon, V.N. Distinct activity of the oxyl Fe^{III}–O group in the methane dissociation by activated iron hydroxide: DFT predictions. *Chem. Phys. Lett.* **2015**, *640*, 94–100. [CrossRef]
67. Dietl, N.; Schlangen, M.; Schwarz, H. Thermal Hydrogen-Atom Transfer from Methane: The Role of Radicals and Spin States in Oxo-Cluster Chemistry. *Angew. Chem. Int. Ed.* **2012**, *51*, 5544–5555. [CrossRef]
68. Pan, J.; Wenger, E.S.; Matthews, M.L.; Pollock, C.J.; Bhardwaj, M.; Kim, A.J.; Allen, B.D.; Grossman, R.B.; Krebs, C.; Bollinger, J.M. Evidence for Modulation of Oxygen Rebound Rate in Control of Outcome by Iron(II)- and 2-Oxoglutarate-Dependent Oxygenases. *J. Am. Chem. Soc.* **2019**, *141*, 15153–15165. [CrossRef]
69. Simons, M.C.; Prinslow, S.D.; Babucci, M.; Hoffman, A.S.; Hong, J.; Vitillo, J.G.; Bare, S.R.; Gates, B.C.; Lu, C.C.; Gagliardi, L.; et al. Beyond Radical Rebound: Methane Oxidation to Methanol Catalyzed by Iron Species in Metal–Organic Framework Nodes. *J. Am. Chem. Soc.* **2021**, *143*, 12165–12174. [CrossRef]

70. Bach, R.D. The DMDO Hydroxylation of Hydrocarbons via the Oxygen Rebound Mechanism. *J. Phys. Chem. A* **2016**, *120*, 840–850. [CrossRef] [PubMed]
71. Goldberg, K.I.; Goldman, A.S. (Eds.) *Activation and Functionalization of C–H Bonds*; American Chemical Society: Washington, DC, USA, 2004.
72. Frisch, M.J.; Trucks, G.W.; Schlegel, H.B.; Scuseria, G.E.; Robb, M.A.; Cheeseman, J.R.; Scalmani, G.; Barone, V.; Petersson, G.A.; Nakatsuji, H.; et al. *Gaussian 16*; Revision C.01; Gaussian Inc.: Wallingford, CT, USA, 2016.
73. Austin, A.; Petersson, G.A.; Frisch, M.J.; Dobek, F.J.; Scalmani, G.; Throssell, K. A Density Functional with Spherical Atom Dispersion Terms. *J. Chem. Theory Comput.* **2012**, *8*, 4989–5007. [CrossRef]
74. Stevens, W.J.; Krauss, M.; Basch, H.; Jasien, P.G. Relativistic compact effective potentials and efficient, shared-exponent basis sets for the third-, fourth-, and fifth-row atoms. *Can. J. Chem.* **1992**, *70*, 612–630. [CrossRef]
75. Becke, A.D. Density-functional thermochemistry. III. The role of exact exchange. *J. Chem. Phys.* **1993**, *98*, 5648–5652.
76. Lee, C.; Yang, W.; Parr, R.G. Development of the Colle-Salvetti correlation-energy formula into a functional of the electron density. *Phys. Rev. B* **1988**, *37*, 785–789. [CrossRef]
77. Zhao, Y.; Truhlar, D.G. The M06 suite of density functionals for main group thermochemistry, thermochemical kinetics, noncovalent interactions, excited states, and transition elements: Two new functionals and systematic testing of four M06-class functionals and 12 other functionals. *Theor. Chem. Acc.* **2008**, *120*, 215.
78. Bosch, E.; Moreno, M.; Lluch, J.M.; Bertrán, J. Intrinsic reaction coordinate calculations for reaction paths possessing branching points. *Chem. Phys. Lett.* **1989**, *160*, 543–548. [CrossRef]
79. Coskun, D.; Jerome, S.V.; Friesner, R.A. Evaluation of the Performance of the B3LYP, PBE0, and M06 DFT Functionals, and DBLOC-Corrected Versions, in the Calculation of Redox Potentials and Spin Splittings for Transition Metal Containing Systems. *J. Chem. Theory Comput.* **2016**, *12*, 1121–1128. [CrossRef] [PubMed]
80. Marenich, A.V.; Cramer, C.J.; Truhlar, D.G. Universal Solvation Model Based on Solute Electron Density and on a Continuum Model of the Solvent Defined by the Bulk Dielectric Constant and Atomic Surface Tensions. *J. Phys. Chem. B* **2009**, *113*, 6378–6396. [CrossRef] [PubMed]
81. Schmidt, M.W.; Gordon, M.S.; Dupuis, M. The intrinsic reaction coordinate and the rotational barrier in silaethylene. *J. Am. Chem. Soc.* **1985**, *107*, 2585–2589. [CrossRef]
82. Santini, C.; Marinelli, M.; Pellei, M. Boron-Centered Scorpionate-Type NHC-Based Ligands and Their Metal Complexes. *Eur. J. Inorg. Chem.* **2016**, *2016*, 2312–2331. [CrossRef]
83. Groom, C.R.; Bruno, I.J.; Lightfoot, M.P.; Ward, S.C. *The Cambridge Structural Databas*, ConQuest Version 2.0.1; CCDC: Cambridge, UK, 2021.
84. Wurzenberger, X.; Piotrowski, H.; Klüfers, P. A Stable Molecular Entity Derived from Rare Iron(II) Minerals: The Square-Planar High-Spin-d6 FeIIO4 Chromophore. *Angew. Chem. Int. Ed.* **2011**, *50*, 4974–4978. [CrossRef]
85. Cao, A.; Nørskov, J.K. Spin Effects in Chemisorption and Catalysis. *ACS Catal.* **2023**, *13*, 3456–3462. [CrossRef]
86. Understanding the Effect of Catalyst Spin State on Reaction. Available online: https://phys.org/news/2024-01-effect-catalyst-state-reaction.html (accessed on 16 December 2024).
87. Rajca, A.; Olankitwanit, A.; Wang, Y.; Boratyński, P.J.; Pink, M.; Rajca, S. High-Spin S = 2 Ground State Aminyl Tetraradicals. *J. Am. Chem. Soc.* **2013**, *135*, 18205–18215. [CrossRef]